Electronic Supplementary Material (ESI) for Materials Horizons.
This journal is © The Royal Society of Chemistry 2023

Supporting Information for

Highly stable and strain-insensitive metal film conductors via manipulating strain distribution

Ting Zhu , Kai Wu *, Yaqiang Wang , Jinyu Zhang , Gang Liu *, Jun Sun *

State Key Laboratory for Mechanical Behavior of Materials, Xi'an Jiaotong University, Xi'an, 710049, P.R. China

** Corresponding authors: msewukai@xjtu.edu.cn;lgsammer@xjtu.edu.cn; junsun@xjtu.edu.cn*

Table of Contents

1. Supporting Information Figures 2

2. Supporting Information Tables 32

3. Supporting Information References 35

1. Supporting Information Figures

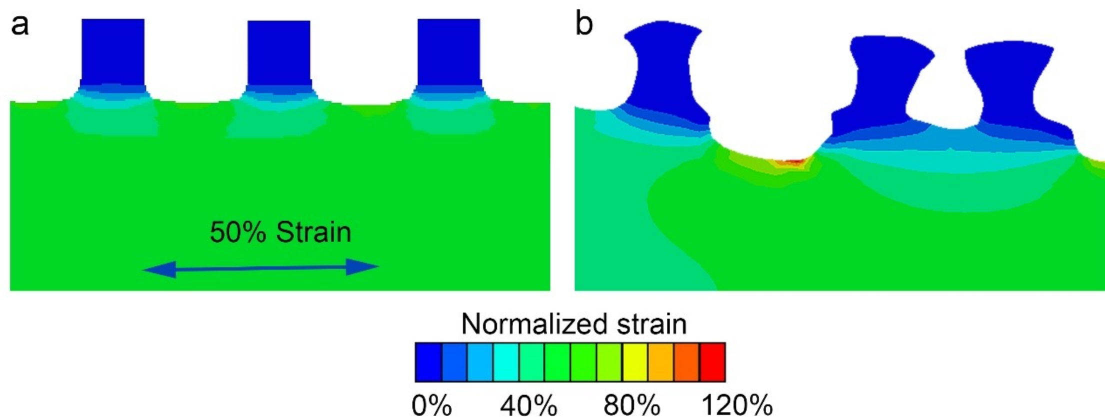

Fig. S1. Enlarged finite element analysis results of strain distribution in the film on (a) microstructured substrates corresponding to the black box in Fig. 1e-II (main text) and (b) hierarchical microstructured substrates corresponding to the purple box Fig. 1e- III (main text).

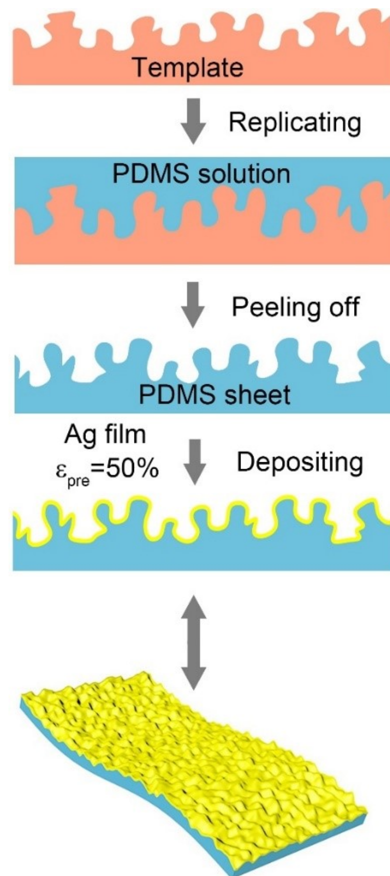

Fig. S2. Schematics of the fabrication process of Ag films on hierarchical microstructured substrates (HMFs).

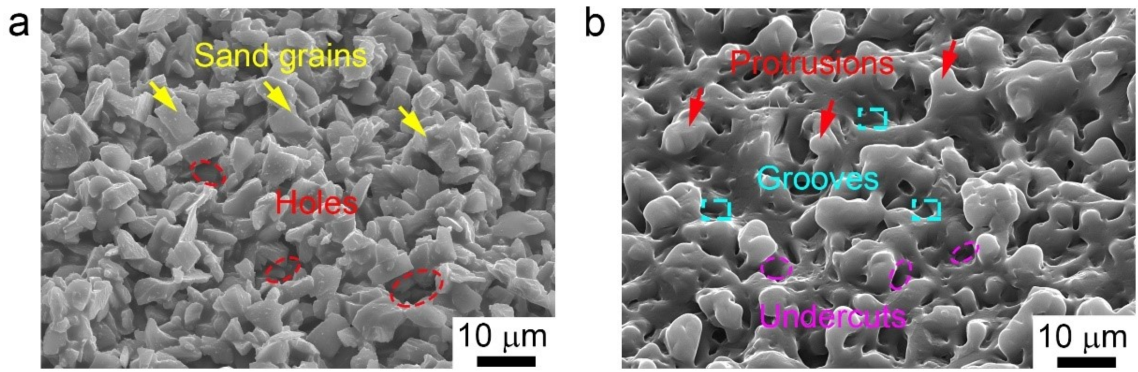

Fig. S3. 45°tilt-view SEM images of (a) sandpaper template and (b) microstructured PDMS sheet.

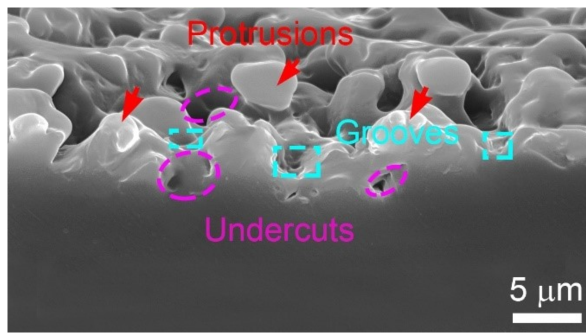

Fig. S4. Cross-sectional SEM image of the microstructured PDMS sheet, corresponding to Fig. 1g (main text).

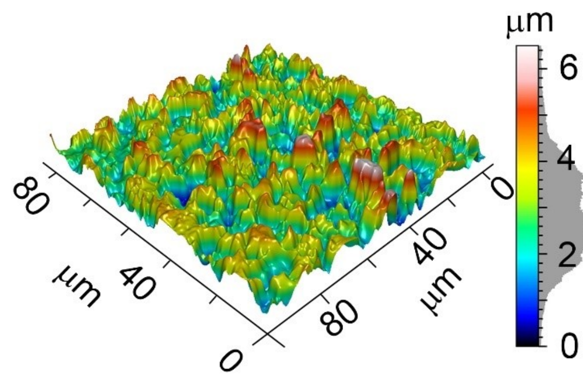

Fig. S5. Three-dimensional CLSM image of the PDMS sheet with protrusions, grooves, and undercuts microstructures.

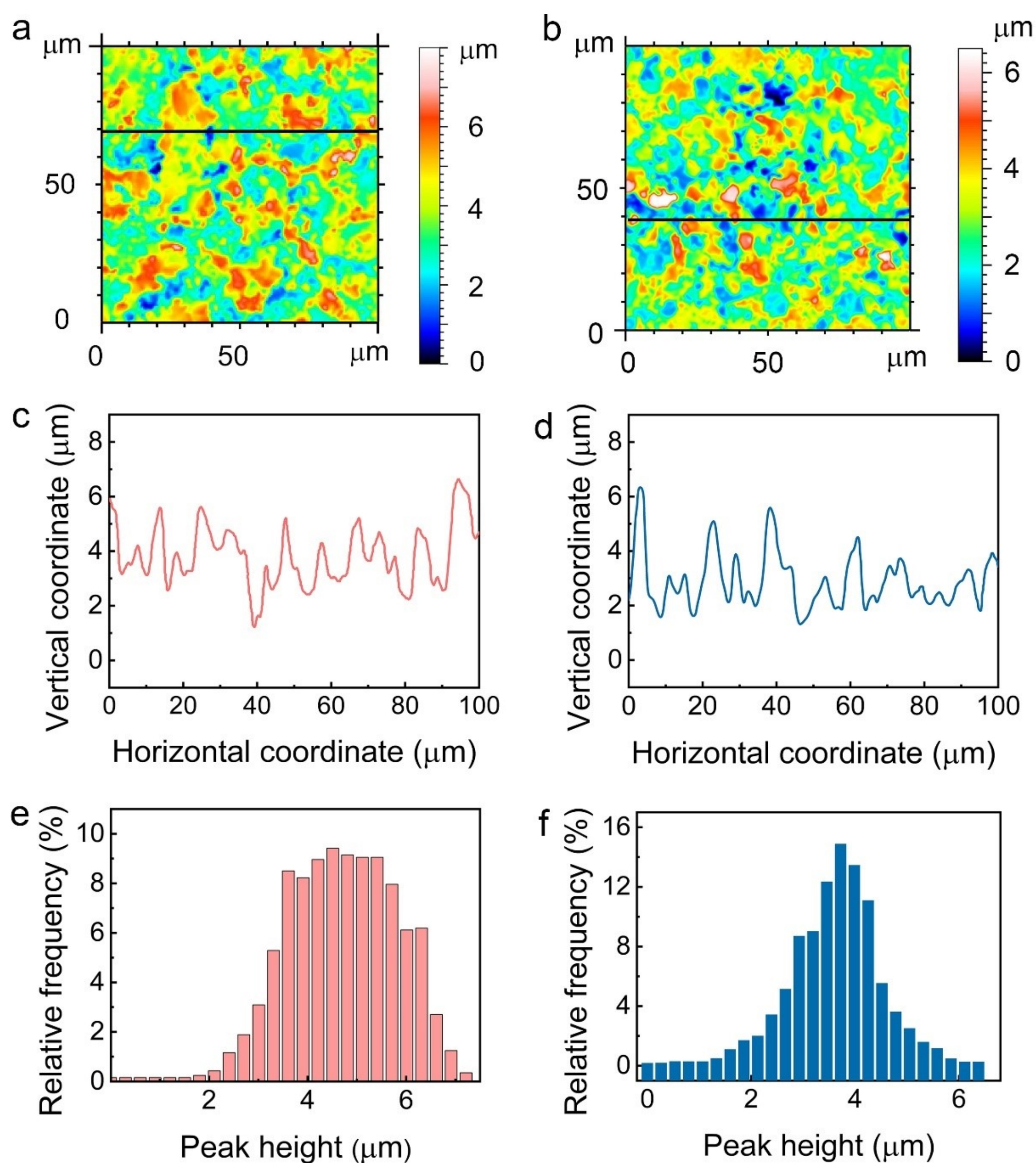

Fig. S6. Topographic images for top view obtained by CLSM analysis for the microstructures of (a) template and (b) PDMS sheet. (c) Height profile corresponding to line scan in (a). (d) Height profile corresponding to line scan in (b). (e) Peak height distribution of microstructures corresponding to (c). (f) Peak height distribution of microstructures corresponding to (d).

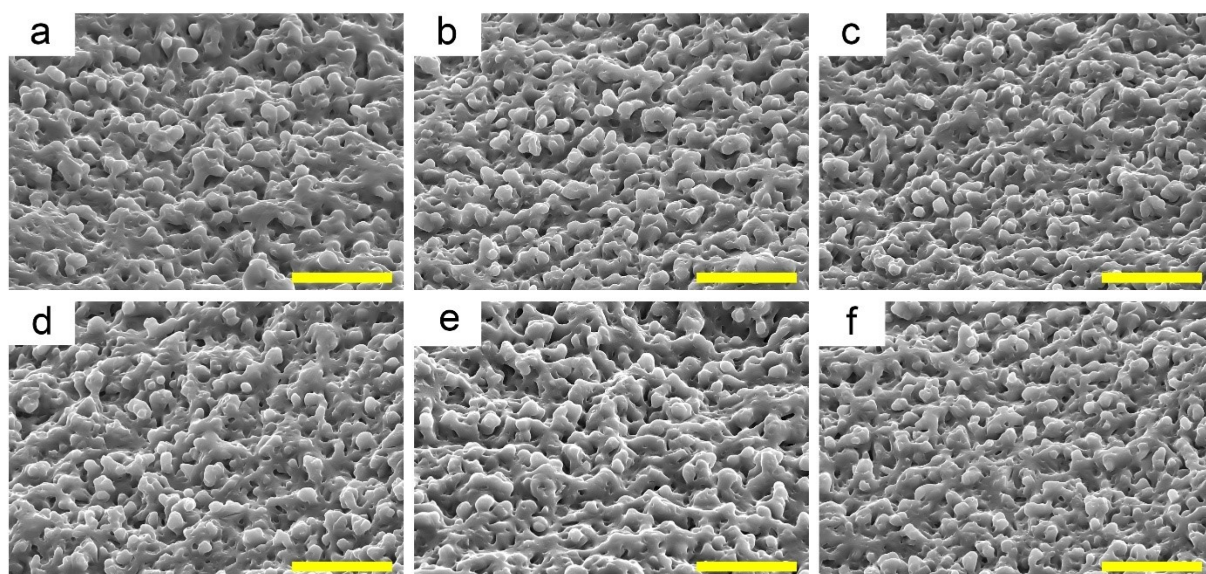

Fig. S7. 45°tilt-view SEM images of the microstructured PDMS sheets replicated from the template: (a) 1st replication; (b) 4th replication; (c) 8th replication; (d) 12th replication; (e) 16th replication; (f) 20th replication (scale bar:20 μm).

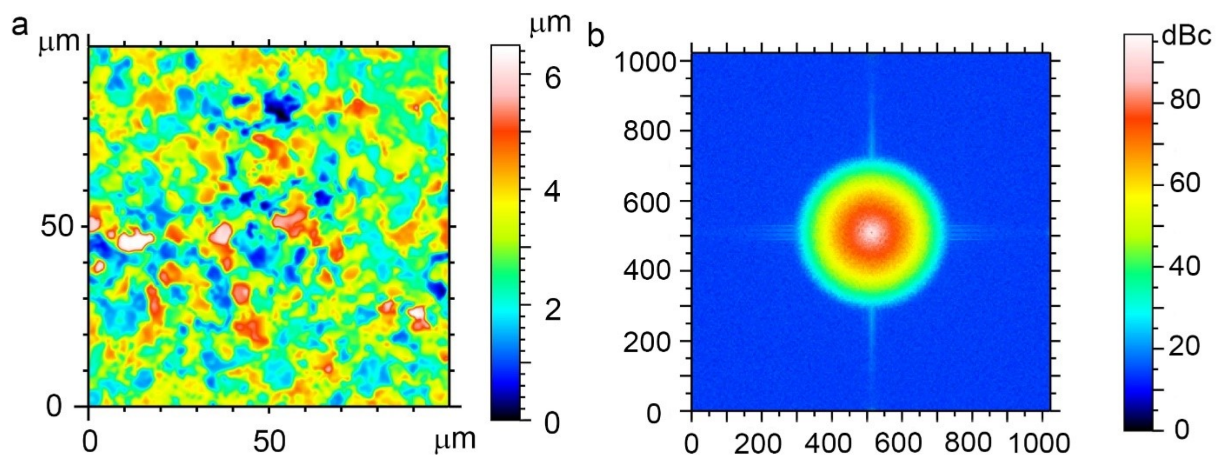

Fig. S8. (a) Top-view CLSM image of surface morphology of the microstructured PDMS sheet. (b) Two-dimensional fast Fourier transform corresponding to (a).

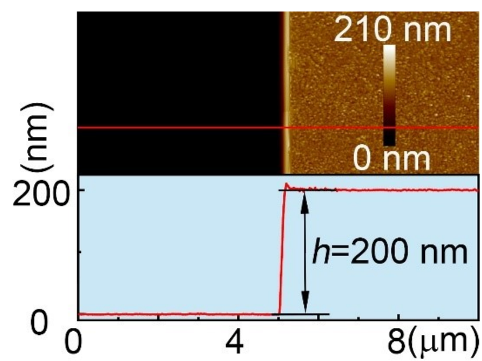

Fig. S9. AFM height image of the deposited 200 nm-thick Ag film on Si wafers.

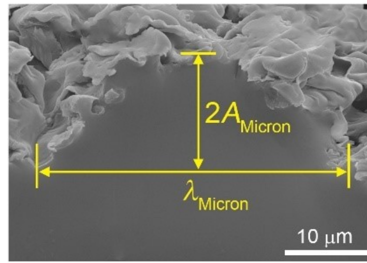

Fig. S10. Cross-sectional SEM image of the micron-scale wrinkle, corresponding to Fig. 1h (main text).

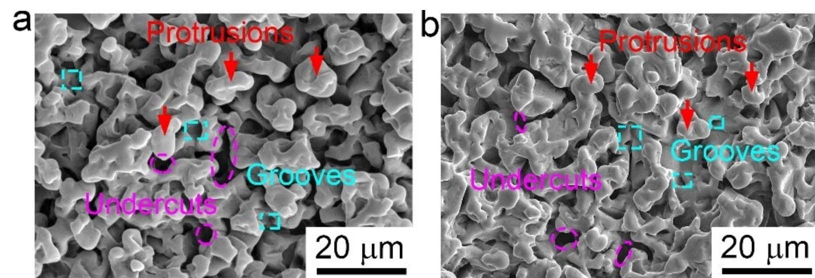

Fig. S11. SEM images of surface microstructures (a) before and (b) after introducing the micron- and submicron-scale wrinkles.

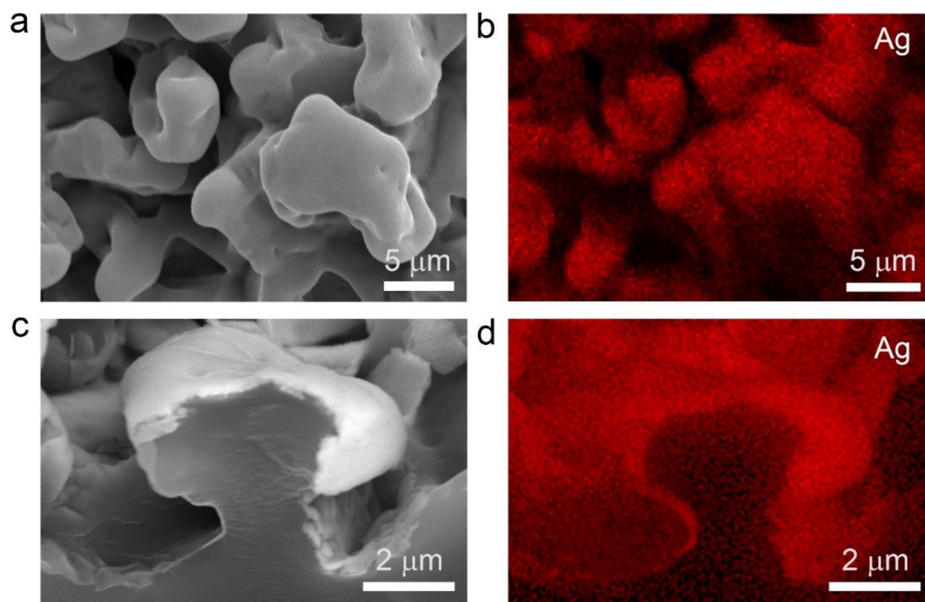

Fig. S12. (a) SEM image and (b) spatial energy dispersive X-ray spectroscopy (EDS) for the 200 nm-thick Ag film on 50% pre-stretched microstructured PDMS sheet. (c) Cross-section SEM image and (d) EDS for the 200 nm-thick Ag on 50% pre-stretched microstructured PDMS sheet.

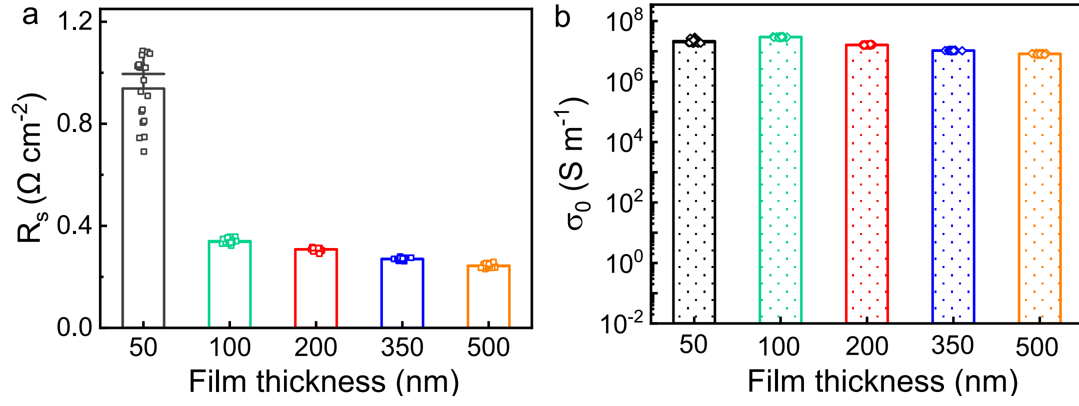

Fig. S13. Variation of (a) sheet resistance (R_s) and (b) initial conductivity (σ_0) of Ag films with film thickness on 50% pre-stretched microstructured PDMS sheets.

Sheet resistance (R_s) can be described by the following equation [1]:

$$R_s = \frac{1}{\sigma h} \tag{1}$$

where σ is conductivity, and h is the thickness of metal film.

Based on Equation. (1), the conductivity (σ) can be calculated as:

$$\sigma = \frac{1}{R_s h} \tag{2}$$

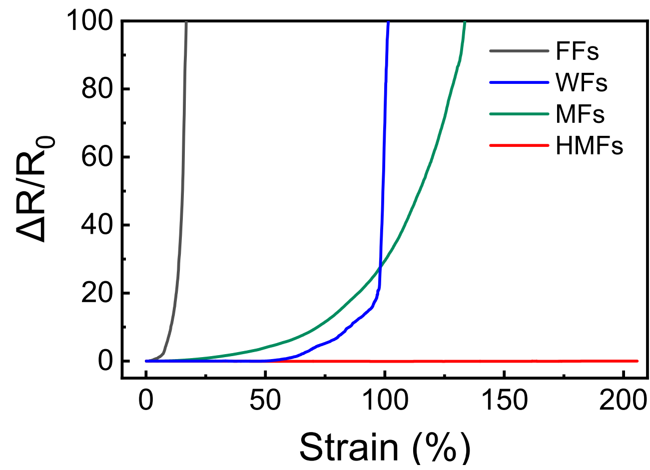

Fig. S14. Relative change resistance ($\Delta R/R_0$) as a function of strain for the Ag films on hierarchical microstructured substrates (HMFs), the Ag films on flat substrates (FFs), the Ag films on microstructured substrate without wrinkles (MFs) and Ag films on wrinkled substrate without microstructures (WFs).

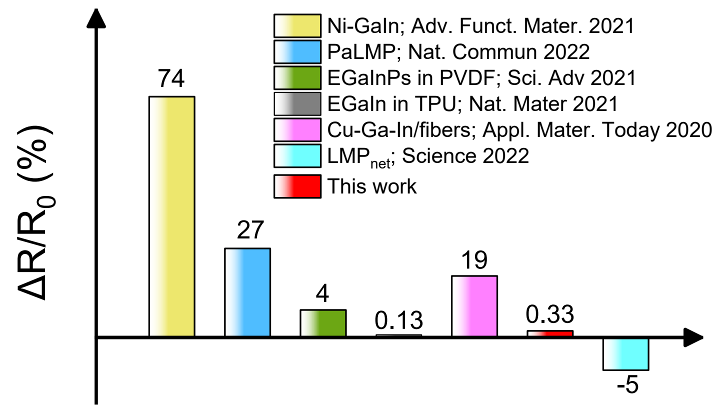

Fig. S15. Comparison of the relative resistance change at 200% strain of this work with previous liquid metal-based stretchable conductor [2-7].

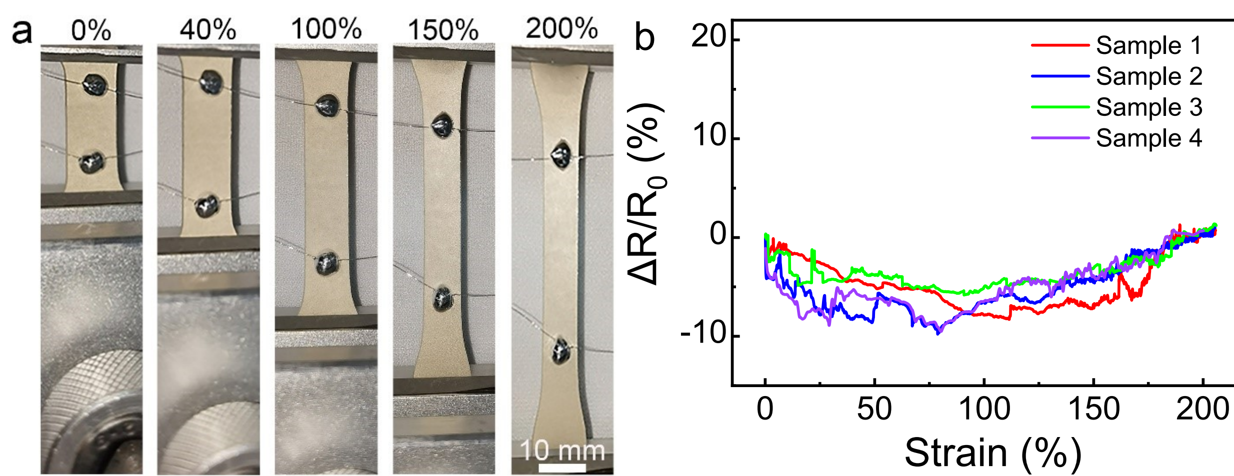

Fig. S16. (a) Digital images of the HWFs at sequential applied tensile strains. (b) Electromechanical performances of the HWFs fabricated simultaneously under the same deposition condition.

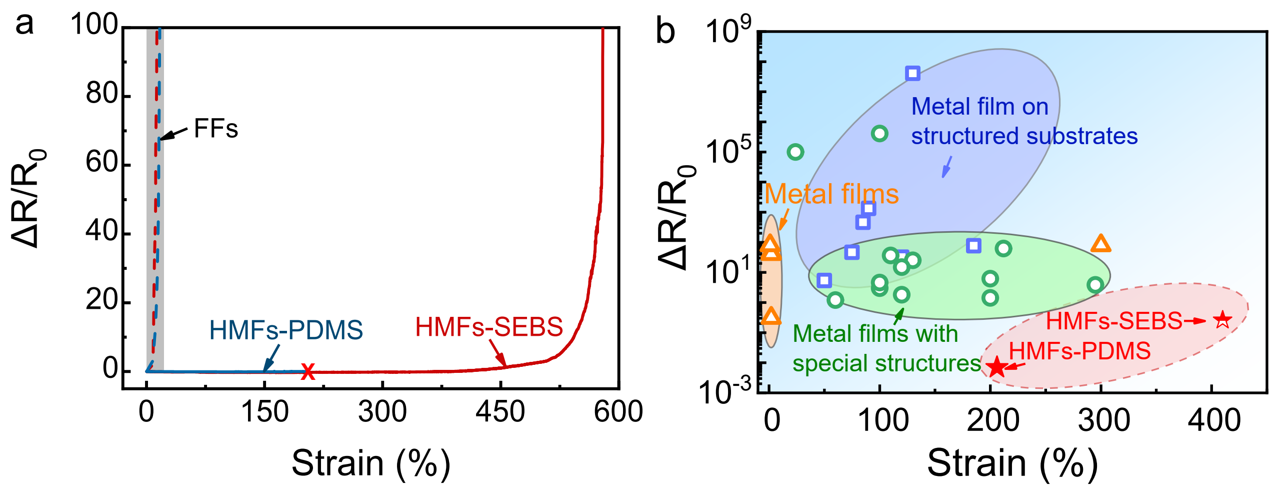

Fig. S17. (a) Relative resistance change ($\Delta R/R_0$) of the different substrates-supported FFs and HMFs as a function of tensile strain. (b) Relative resistance change versus stretchability of HMFs, in comparison with other metal-based stretchable conductors [8-32].

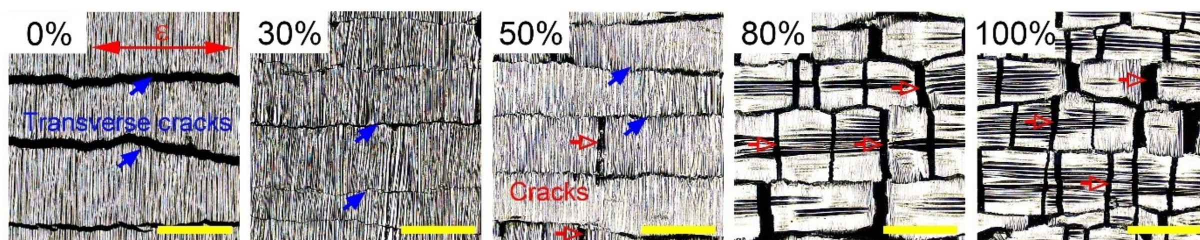

Fig. S18. CLSM images of the surface morphologies of the WFs at sequential strains, illustrating the cracking process (scale bar:200 μm).

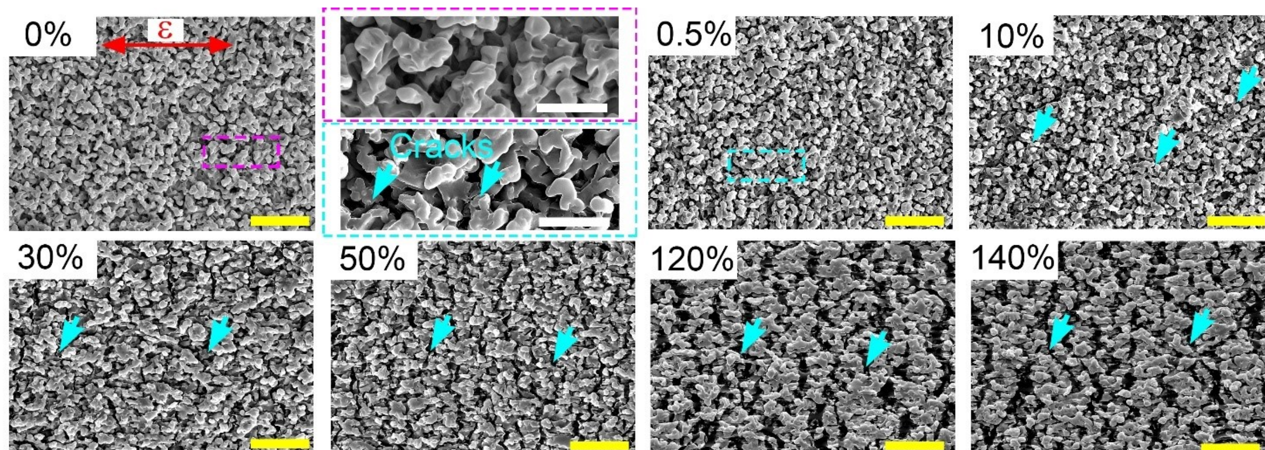

Fig. S19. SEM images of the surface morphologies of the MFs at sequential strains, illustrating the cracking process (yellow scale bar: 200 μm; white scale bar: 20 μm).

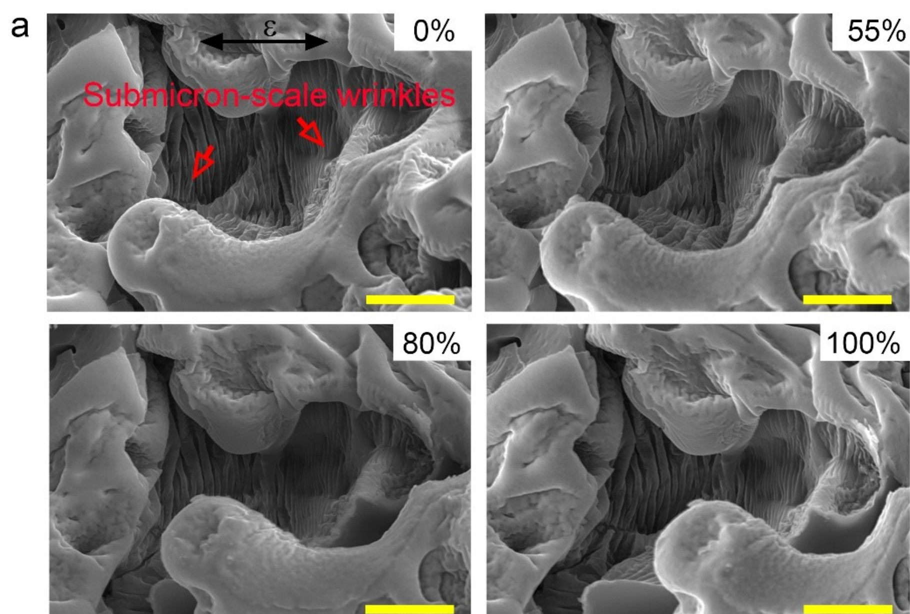

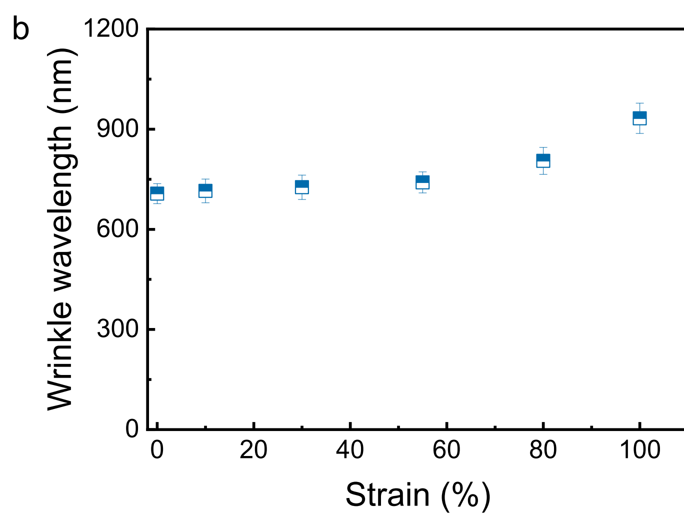

Fig. S20. (a) SEM images of the submicron-scale wrinkles at an undercut under sequential strains (scale bar: 5 μm). (b) Evolution of average wrinkle wavelength with applied strain for submicron-scale wrinkles.

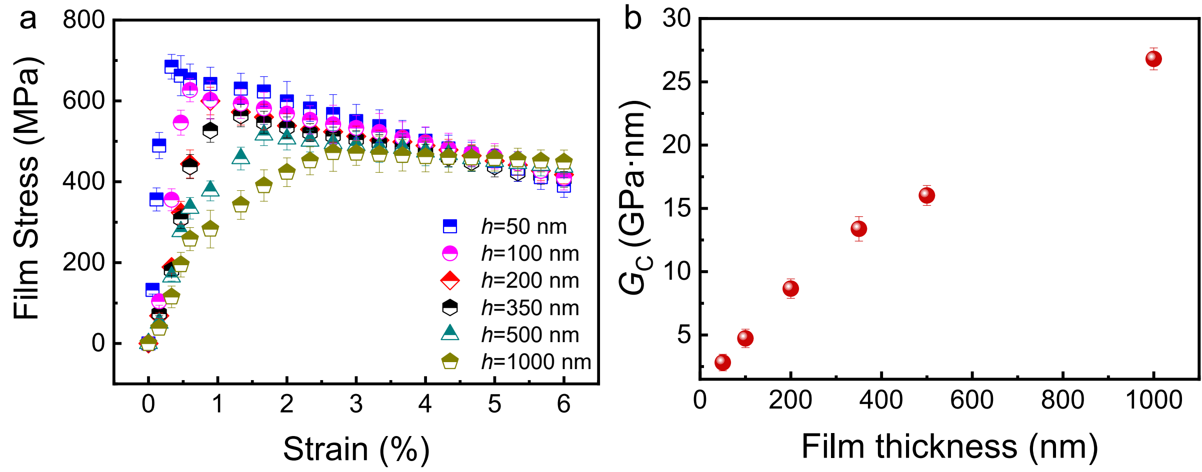

Fig. S21. (a) Evolution of film stress with applied strain for Ag films with different film thicknesses on flat PDMS substrates. (b) Variation of critical energy release rate G_C with film thickness for Ag films on flat PDMS substrates.

According to the linear elastic fracture mechanics, the steady state crack propagation can be described analytically by two-dimensional models [33]. The critical energy release rate G_C associated with the steady-state crack propagation in a brittle film (such as nanocrystalline metal film) on a substrate is given by [33]:

$$G = \frac{\pi \sigma^2 h}{2E_f}(1-\nu_f^2)g(\alpha,\beta) \tag{1}$$

where σ is the fracture stress of the film which can be determined from the stress-strain curve obtained by synchrotron X-ray diffraction, h is the film thickness, E_f is the elastic modulus of the film, ν_f is the Poisson's ratio of the film, and $g(\alpha,\beta)$ is a dimensionless parameter depending on the Dundurs parameters (α and β). The formulas for α and β are as follows:

$$\alpha = \frac{\overline{E}_f - \overline{E}_s}{\overline{E}_f + \overline{E}_s} \tag{2}$$

$$\beta = \frac{\mu_f(1-2\nu_s) - \mu_s(1-2\nu_f)}{2\mu_f(1-\nu_s) + 2\mu_s(1-\nu_f)} \tag{3}$$

where $\overline{E}=\frac{E}{1-\nu^2}$, μ is the shear modulus and the subscripts f and s denote the film and the substrate, respectively.

Substitution of these values (Table S3) into the above equations, we calculated the critical energy release rate of Ag films with different film thicknesses (Fig. S21b). If the energy release rate G in film exceeds the critical value G_C, the crack will propagate. When $G < G_C$, the crack arrests.

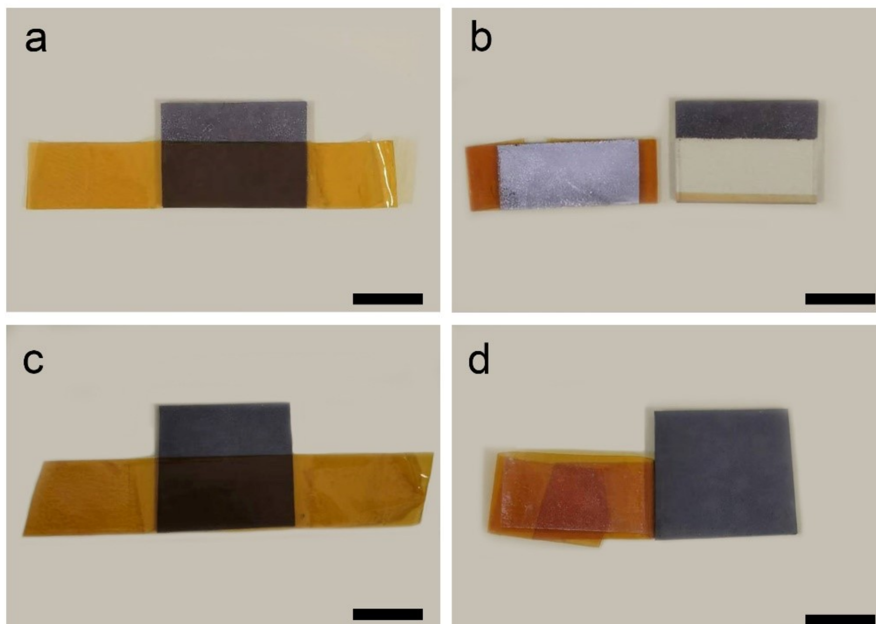

Fig. S22. Adhesion measurement by Kapton tape peel test. (a-b) FFs and (c-d) HMFs (scale bar: 5 mm).

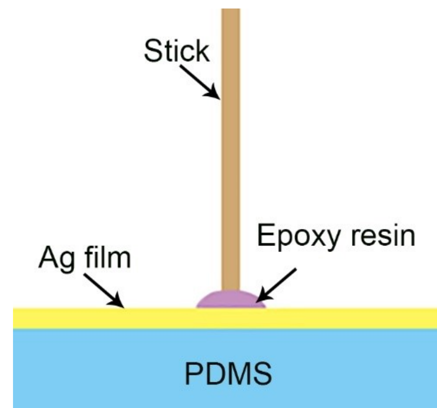

Fig. S23. Schematic of the experimental setup by pull-out test.

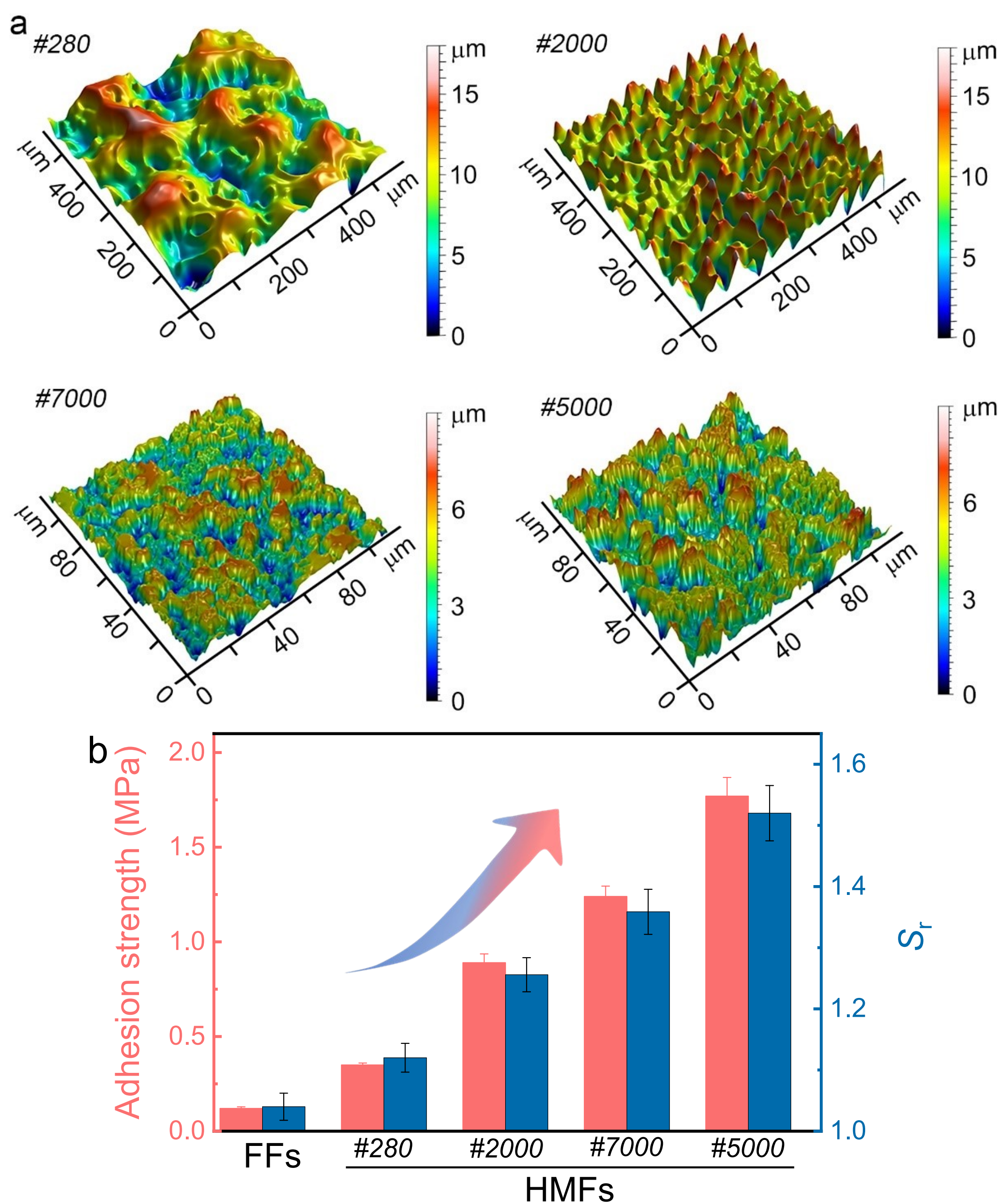

Fig. S24. (a) Three-dimensional CLSM images of the microstructured PDMS sheets molded from different sandpapers. (b) Interfacial adhesion strength and area ratio S_r for Ag films on plat PDMS substrates and microstructured PDMS substrates. In this work, the #5000 sandpaper with better interfacial adhesion strength is selected as the template to fabricate the metal film-based stretchable conductor and explore the electromechanical performances.

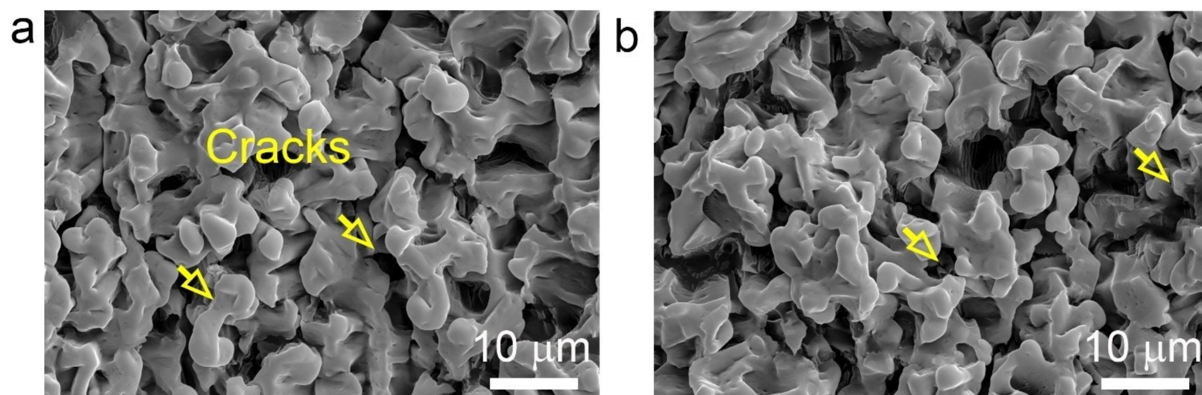

Fig. S25. SEM images of the surface morphologies of HMFs before and after 15000 cycles at 100%.

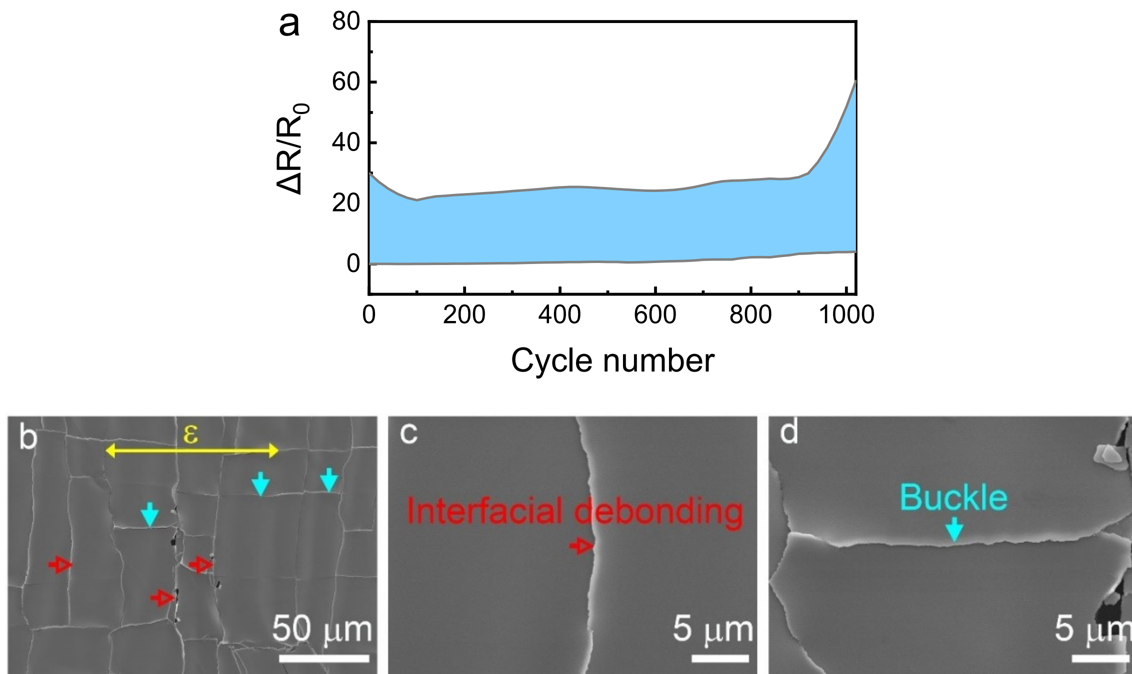

Fig. S26. (a) Relative resistance change versus cycle number at 10% strain. (b) SEM image morphology of the FFs after 1000 cycles at 10% strain. (c) Enlarged image of the interfacial debonding along the cracks. (d) Enlarged image of a buckle (delaminated region between two cracks).

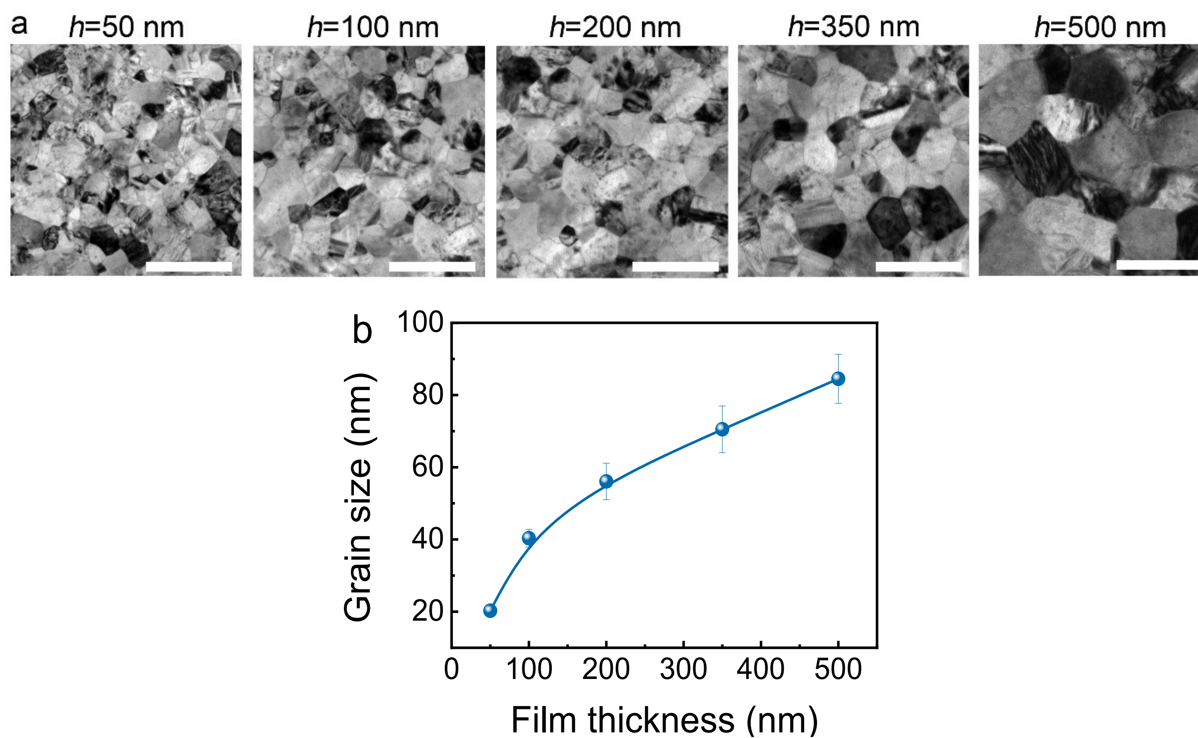

Fig. S27. (a) TEM images of Ag films with different thicknesses (scale bar: 100 nm). (b) Dependence of average grain size on film thickness measured by TEM.

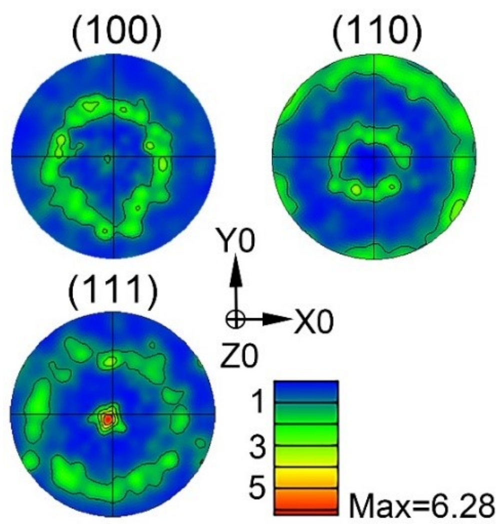

Fig. S28. Pole figures of 200 nm-thick Ag film, corresponding to Fig. 3f (main text).

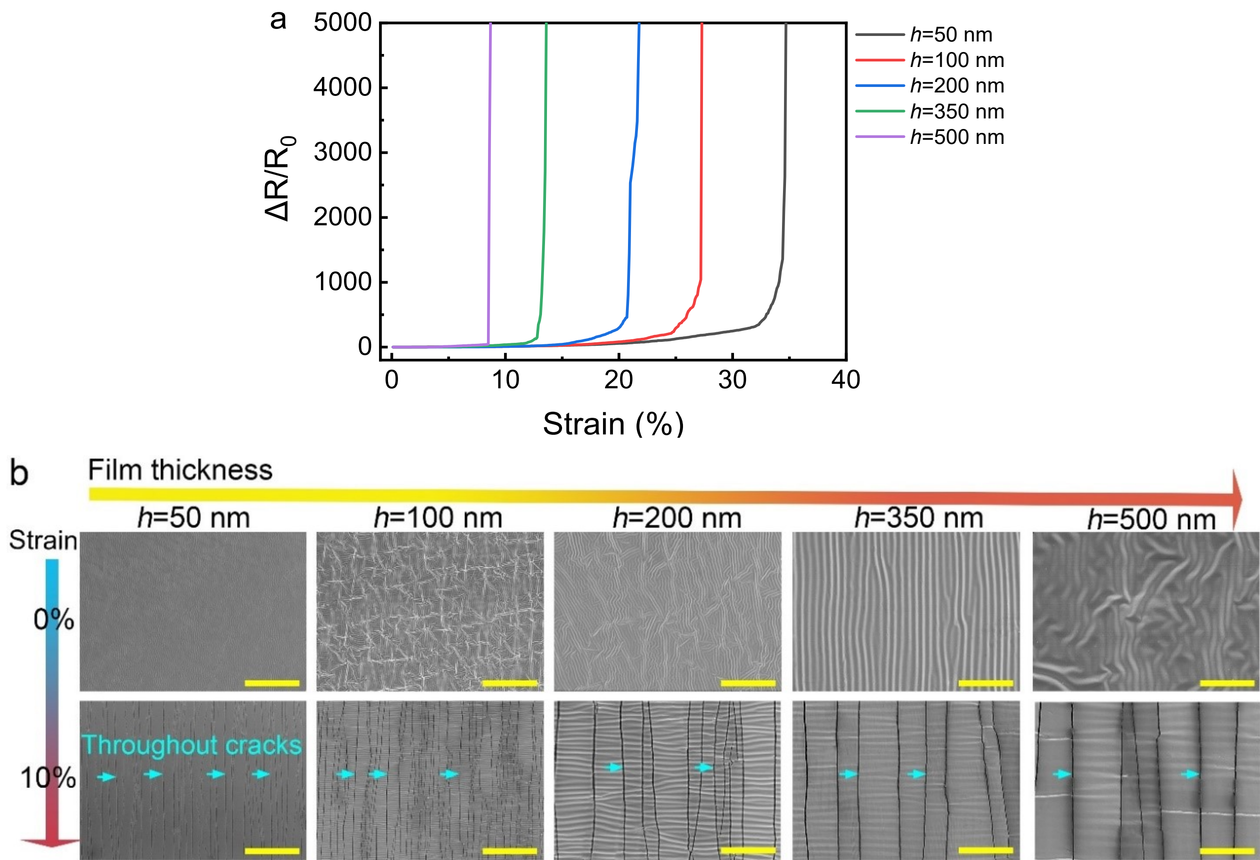

Fig. S29. (a) Variation of relative resistance change with applied strain for the FFs with different thicknesses. (b) SEM images of surface morphologies of the FFs with different thicknesses at 0% and 10% (scale bar: 300 μm). The local energy release rate G (the crack propagation driving force) and the critical energy release rate G_C increase monotonically with the increase of film thickness. Obviously, for FFs, the monotonic decrease of the stretchability with the increase of film thickness because the film always has a higher crack propagation driving force ($G > G_C$).

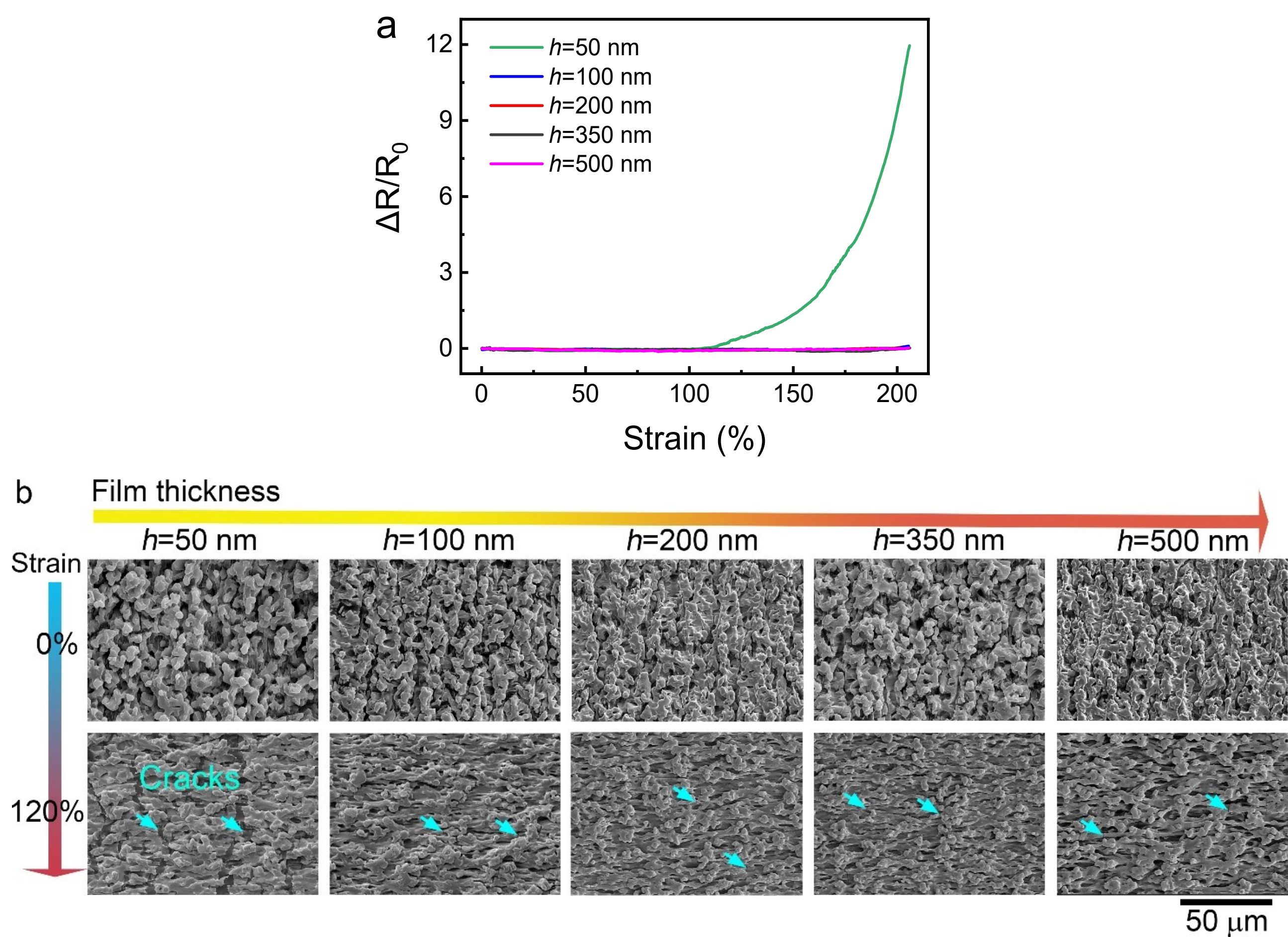

Fig. S30. (a) Variation of relative resistance change with applied strain. (b) SEM images of surface morphologies of the HMFs with different thicknesses at 0% and 120%.

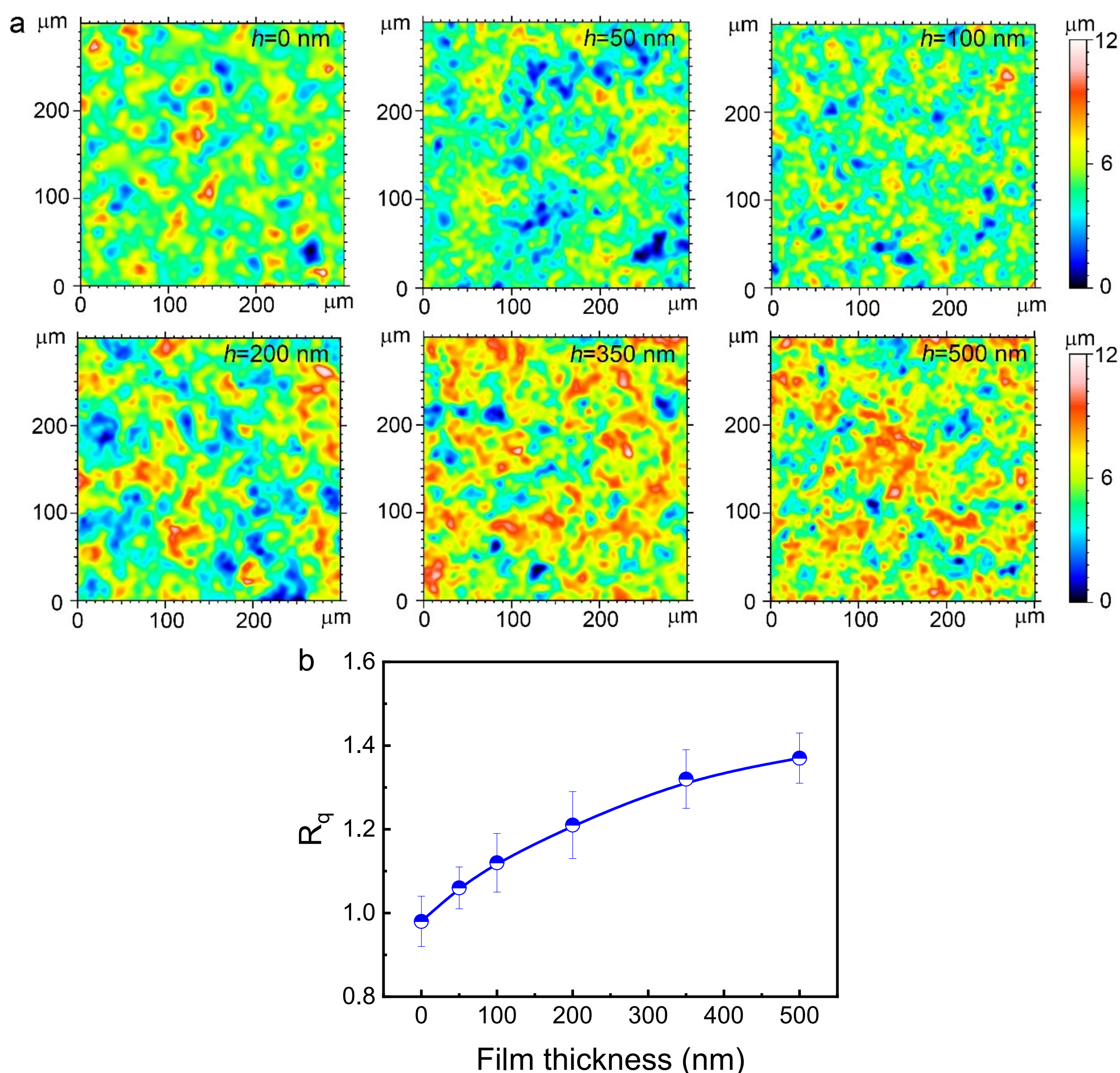

Fig. S31. (a) Topographic images for top view obtained by CLSM analysis for the microstructures of Ag films with different thicknesses sputtered on the microstructured PDMS sheet. (b) Dependence of surface roughness parameter Rq on Ag film thickness. The increase of surface irregularities with film thickness can be attributed to the shadowing effect induced by surface protrusions [34, 35].

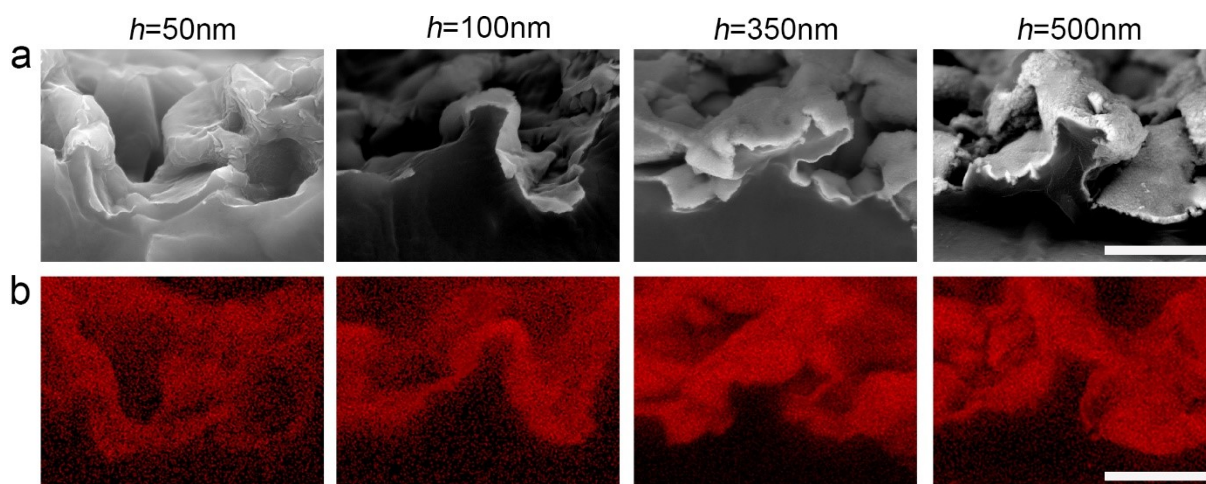

Fig. S32. (a) Cross-sectional SEM images and (b) EDS for the HMFs with different thicknesses (scale bar:5 μm).

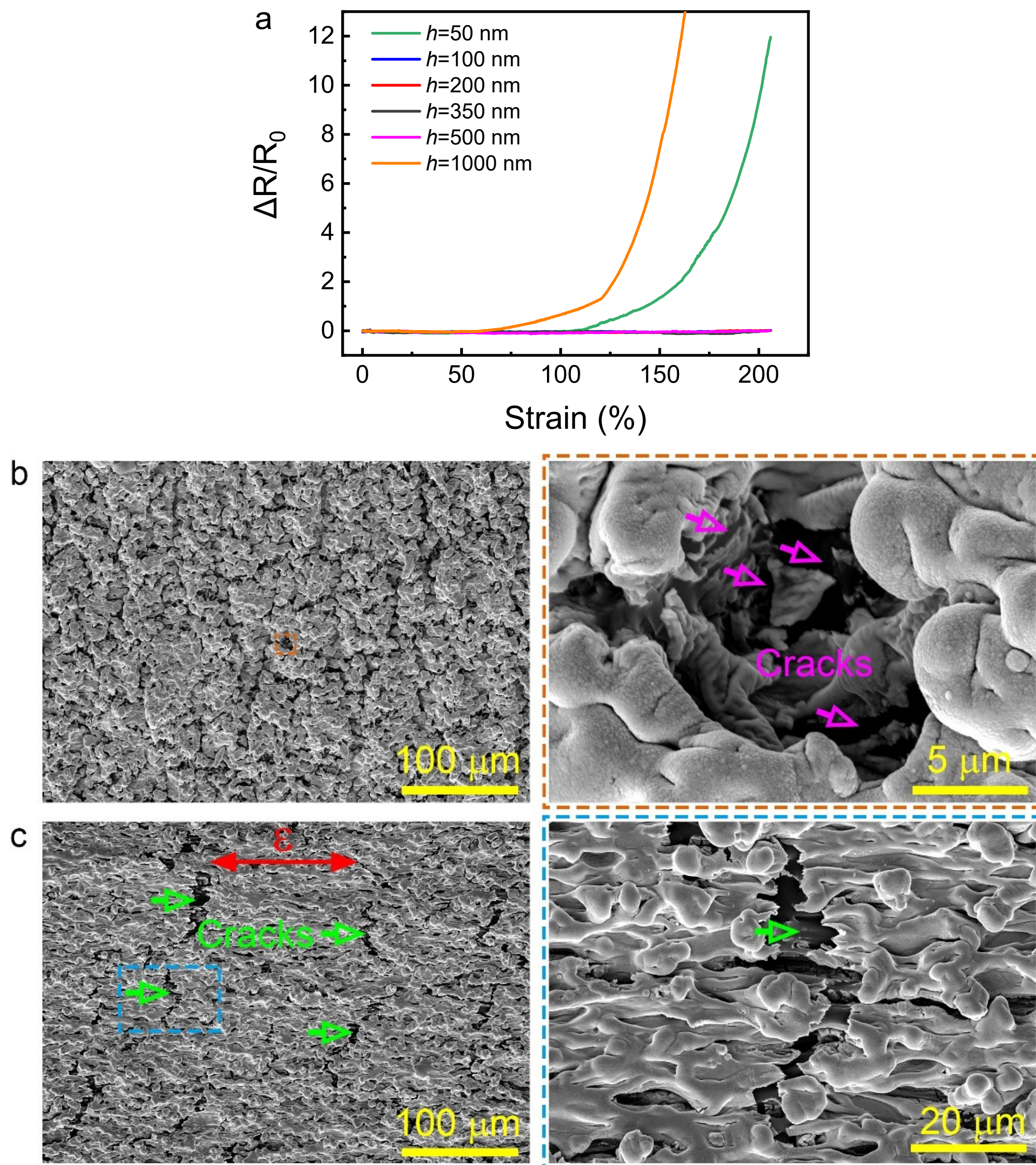

Fig. S33. (a) Variation of relative resistance change with applied strain for microstructured Ag films with different film thickness h. SEM images of the surface morphologies of microstructured Ag films with h = 1000 nm at (b) 0% and (c) 120%.

It is revealed that many cracks, instead of wrinkles, were formed at the undercuts after film deposition and prestrain relaxation. According to the nonlinear buckling theory [2, 4, 39], the wrinkle dimension (wavelength) scales with the film thickness. The undercut regions have insufficient room to accommodate the periodic wrinkles for the thick film (e.g., h = 1000 nm). Releasing the prestrain

applies a compressive stress to the metal film, leading to film bending. The excessive tensile strain at the top of wrinkle caused by bending will trigger the film cracking. Upon stretching, these cracks at the undercuts will propagate and merge into the long crack (Figure S33c), which impairs the stretchability of Ag film.

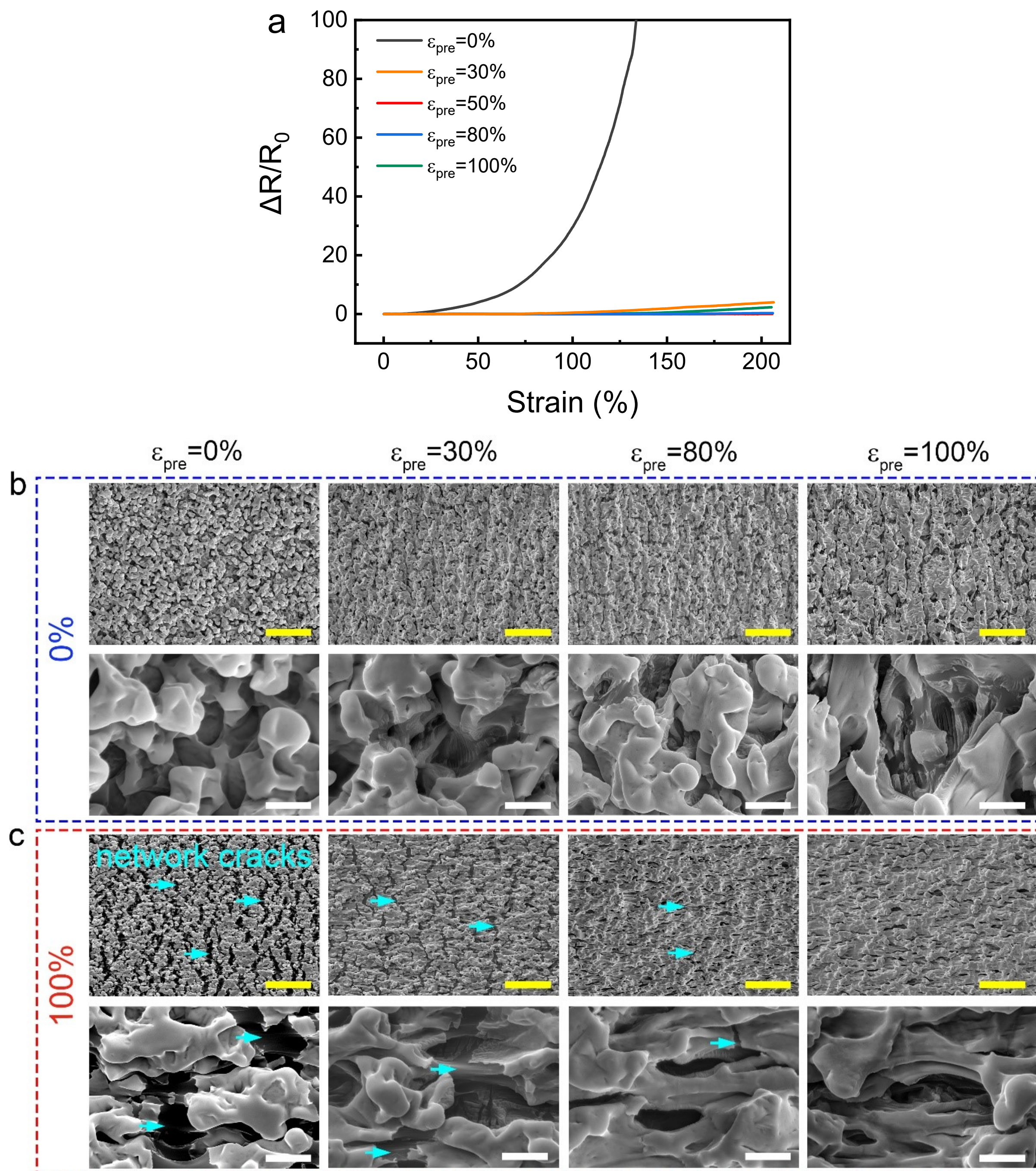

Fig. S34. (a) Variation of relative resistance change with applied strain for 200 nm-thick HMFs fabricated by different substrate pre-strains. SEM images of surface morphologies of the HMFs fabricated by different substrate pre-strains at (b) 0% and (c)100% (yellow scale bar: 50 μm; white scale bar: 5 μm).

1

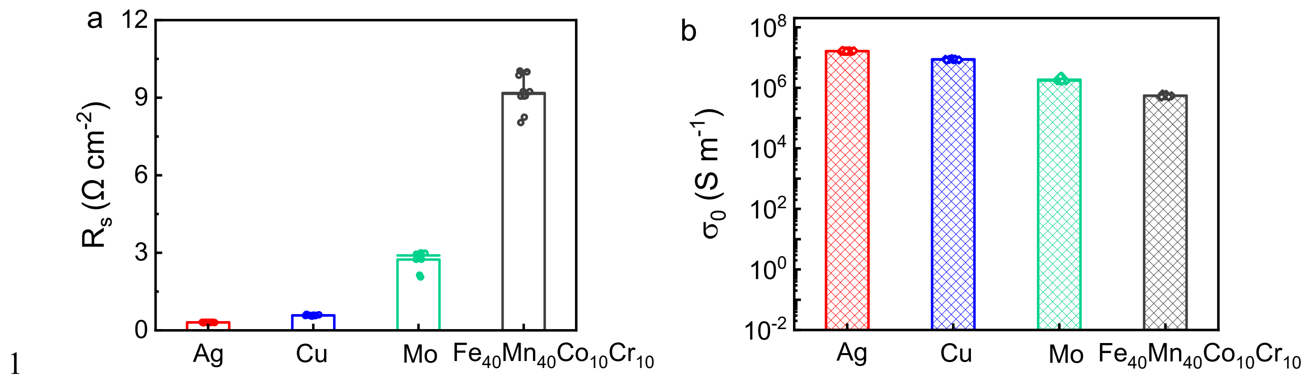

2 **Fig. S35.** (a) Sheet resistance (R_s) and (b) initial conductivity (σ_0) of 200 nm-thick metal films (Ag,
3 Cu, Mo, and $Fe_{40}Mn_{40}Co_{10}Cr_{10}$) on hierarchical microstructured substrates. Generally, the electrical
4 resistivity is related to microstructural defects (e.g., vacancies, dislocations, and grain boundaries)
5 and lattice distortions, which reduce the electron mean free path and lead to electron scattering [36 37].
6 The $Fe_{40}Mn_{40}Co_{10}Cr_{10}$ alloy film exhibits the highest sheet resistance because of the combined effect
7 of smaller grain size (more grain boundaries) and the severe lattice distortion (highly-concentrated
8 point defects) [38].

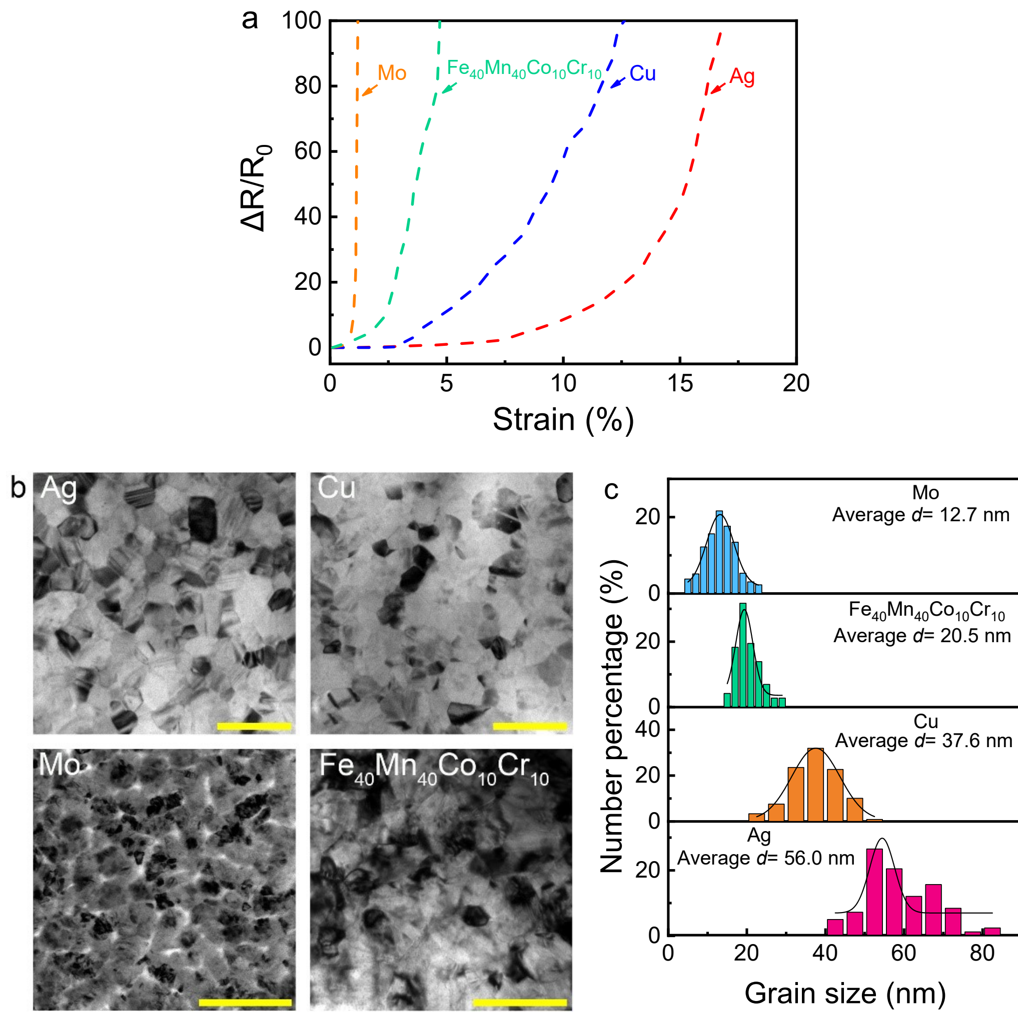

Fig. S36. (a) Electromechanical performances for various metal films on PDMS substrates without hierarchical microstructures. (b) TEM images of Ag films with various $h = 200$ nm metal films (scale bar: 100 nm). (c) Grain size distributions for various metal films.

Mo has body-centered cubic (BCC) structure, while Ag, Cu, and $Fe_{40}Mn_{40}Co_{10}Cr_{10}$ have face centered cubic (FCC) structure. FCC crystal is more ductile than BCC crystal because of the higher Peierls-Nabarro stress in BCC crystals as compared to FCC crystals [39, 40]. Thus, the Mo film exhibits the lowest stretchability.

We performed transmission electron microscopy (TEM) to observe the microstructural features

of metal films with h = 200 nm (Fig. S36b). Statistical results (Fig. S36c) indicate that the average grain size is 56.0 nm for Ag, 37.6 nm for Cu, 20.5 nm for $Fe_{40}Mn_{40}Co_{10}Cr_{10}$, and 12.7 nm for Mo. The stretchability of nanocrystalline metal films generally decreases with reducing grain size, because of dimensional constraints on dislocation activity [41]. Therefore, Ag film exhibits highest stretchability. Compared with Ag and Cu, the $Fe_{40}Mn_{40}Co_{10}Cr_{10}$ alloy has a lower stretchability, because the severe lattice distortion strongly hinders the dislocation movement [42-44].

2. Supporting Information Tables

Table S1. CLSM roughness analysis of the surface microstructures of sandpaper template and PDMS sheet (scan sizes: 10 × 10 μm).

	R_q (μm)	R_a (μm)	R_{max} (μm)	R_{sk}	R_{ku}	R_{sm} (μm)	R_{pc} (1/mm)
Sandpaper template	1.11±0.09	0.90±0.05	5.72±1.35	0.24±0.06	2.51±0.84	20.60±2.43	48.54±6.43
PDMS sheet	0.96±0.06	0.78±0.04	5.82±1.15	0.37±0.07	3.15±0.93	17.56±1.75	56.95±8.16

International standard ISO 21920 is used for roughness analysis. Those parameters are as follows: average roughness (R_a), root mean squared roughness (R_q), maximum roughness (R_{max}), skewness (R_{sk}), kurtosis (R_{ku}), mean width of profile elements (R_{sm}), and peak counts (R_{pc}).

Table S2. Comparison of the stretchability, the relative resistance change and stability with other stretchable metal-based conductors.

Materials	ε_{max} **(%)**	$\Delta R/R_0$ **at max strain**	**Stability (Number of cycles)**	**Ref.**
Ag/PDMS	200	6.20	N.A.	[8]
Au/P-PDMS	120	32	1000@1%	[9]
Ag-Cr-Cu-EGaIn/PDMS	85	461	1100@40%	[10]
Au/PDMS	24	100000	10000@11%	[11]
Au/PDMS	90	1330	100@60%	[12]
Pt/PDMS	130	4.1E7	N.A.	[13]
Au/PDMS	120	0.14	10000@50%	[14]
Au+Au NWs/PDMS	60	1.20	1000@60%	[15]
Au/PDMS	100	3	5000@50%	[16]
Pt/Silk	110	36.50	100@20%	[17]
Cu-Cr/PDMS	50	5.40	1000@50%	[18]
Cu/PDMS	75	46.50	1000@50%	[19]
Cu/PDMS	100	408475	10000@40%	[21]
Au+Au NWs/SEBS fiber	200	1.43	5000@50%	[20]
Au/Semi-polymerized PDMS	130	25.25	>10000@60%	[22]
Pt/PU	2	41	5000@2%	[23]
Pt/PU	2	46	10000@2%	[24]
Cu-Al/PI	2	0.31	N.A.	[25]
Au/PDMS	1	80	N.A.	[26]
Pt/MPTMS	185	77	1000@50%	[27]
Ag-FeO_x/PDMS	295	3.85	>900@40%	[28]
Au/PDMS	300	80	5000@100%	[29]
Au/SEBS	212	62	>600@20%	[30]
Au/ $PDMS_{0.9}$-IPDI	100	4.6	1000@50%	[31]
Au/SEBS	120	15	1000@40%	[32]
Ag/PDMS	**206**	**0.007**	**>15000@100%**	**This work**
Ag/SEBS	**410**	**0.26**	**N.A.**	**This work**

Table S3. Summary of relevant parameters for the calculation of critical energy release rate.

h (nm)	σ (MPa)	E_s (MPa)	E_f (GPa)	v_s	v_f	α	β	$g(\alpha,\beta)$	G_C (GPa•nm)
50	684.56	2.20	71	0.50	0.38	0.99	0.25	9.98	2.82
100	626.85	2.20	71	0.50	0.38	0.99	0.25	9.98	4.73
200	599.81	2.20	71	0.50	0.38	0.99	0.25	9.98	8.66
350	563.68	2.20	71	0.50	0.38	0.99	0.25	9.98	13.38
500	515.99	2.20	71	0.50	0.38	0.99	0.25	9.98	16.02
1000	472.44	2.20	71	0.50	0.38	0.99	0.25	9.98	26.81

Table S4. Comparison of the initial conductivity, the stretchability, the relative resistance change and the quality factor with other stretchable conductors.

Materials	ε_{max} **(%)**	σ_0 **(S m^{-1})**	$\Delta R/R_0$ **at max strain**	Q **at max strain**	**Stability (Number of cycles)**	**Ref.**
CNT in fluorine rubber	134	5700	51	0.03	4000@25%	[45]
LMPs in elastomeric matrix	500	2100000	0.31	16.29	8000@300%	[7]
LM sheath-core microfibers	740	43500	4	1.85	600@100%	[4]
bGaIn/VHB	1200	2060000	4	3	1500@500%	[46]
Ag flakes in fluorine rubber	400	400000	106	0.04	100@50%	[47]
PEDOT:PSS	800	100000	4482	0.002	1000@100%	[48]
AgNWs/Au in SBS	840	3000000	2649	0.003	3000@30%	[49]
Graphene/PU	1010	124	0.90	11.26	>4000@10%	[50]
(PEDOT/PSS/PBP)/ TPE	900	8000	0.03	290	1766@300%	[51]
Ag flakes PAAm alginate hydrogel	250	37400	70	0.04	1000@100%	[52]
Ag NPs in TPU	115	1100000	20.20	0.06	10000@5%	[53]
EGaIn droplets dispersed in PDMS	50	137000	0.04	11.60	1000@50%	[54]
Au film deposited on PDMS	100	41100000	0.03	33	5000@50%	[16]
CNT/Ecoflex	200	0.56	0.07	28.57	N.A.	[55]
Au/PDMS	50	11000	0.07	17.86	3000@50%	[56]
EGaIn-rich layer on SEBS	250	1200000	1.70	1.47	>100@200%	[57]
Au/PDMS	300	1600000	77	0.039	5000@100%	[29]
Graphene/PDMS	90	1000	200	45	N.A.	[58]
PEDOT:PSS/PVA DN hydrogel	100	1000	1.20	0.83	1000@100%	[59]
Cu-LM/SIS	1200	1200000	37.10	32.34	1000@300%	[60]
Ag nanomaterials	50	3100000	0.0026	192	1000@50%	[1]
Ag/PDMS	**206**	**17000000**	**0.007**	**288.05**	**>15000@100%**	**This work**

3. Supporting Information References

1. D. Jung, C. Lim, C. Park, Y. Kim, M. Kim, S. Lee, H. Lee, J. H. Kim, T. Hyeon and D. H. Kim, *Adv. Mater.*, 2022, **34**, e2200980.
2. X. P. Hao, C. Y. Li, C. W. Zhang, M. Du, Z. Ying, Q. Zheng and Z. L. Wu, *Adv. Funct. Mater.*, 2021, **31**, 2105481.
3. G. H. Lee, Y. R. Lee, H. Kim, D. A. Kwon, H. Kim, C. Yang, S. Q. Choi, S. Park, J. W. Jeong and S. Park, *Nat Commun*, 2022, **13**, 2643.
4. L. Zheng, M. Zhu, B. Wu, Z. Li, S. Sun and P. Wu, *Sci Adv*, 2021, **7**, eabg4041.
5. Z. Ma, Q. Huang, Q. Xu, Q. Zhuang, X. Zhao, Y. Yang, H. Qiu, Z. Yang, C. Wang, Y. Chai and Z. Zheng, *Nat Mater*, 2021, **20**, 859-868.
6. R. Guo, H. Wang, G. Chen, B. Yuan, Y. Zhang and J. Liu, *Appl. Mater. Today*, 2020, **20**, 100738.
7. W. Lee, H. Kim, I. Kang, H. Park, J. Jung, H. Lee, H. Park, J. S. Park, J. M. Yuk, S. Ryu, J.-W. Jeong and J. Kang, *Science* 2022, **378**, 637-641.
8. B. Feng, T. Sun, W. Wang, Y. Xiao, J. Huo, Z. Deng, G. Bian, Y. Wu, G. Zou, W. Wang, T. Ren and L. Liu, *Adv. Mater.*, 2022, **35**, e2208568.
9. J. Zhu, X. Wu, J. Jan, S. Du, J. Evans and A. C. Arias, *ACS Appl. Mater. Interfaces*, 2021, **13**, 38105-38113.
10. B. Feng, X. Jiang, G. Zou, W. Wang, T. Sun, H. Yang, G. Zhao, M. Dong, Y. Xiao, H. Zhu and L. Liu, *Adv. Funct. Mater.*, 2021, **31**, 2102359.
11. C. Cho, P. Kang, A. Taqieddin, Y. Jing, K. Yong, J. M. Kim, M. F. Haque, N. R. Aluru and S. Nam, *Nat Electron*, 2021, **4**, 126-133.
12. J. Shi, S. Lv, L. Wang, Z. Dai, S. Yang, L. Zhao, H. Tian, M. Du, H. Li and Y. Fang, *ACS Appl. Mater. Interfaces*, 2019, **6**, 1901223.
13. W. Miao, Y. Yao, Z. Zhang, C. Ma, S. Li, J. Tang, H. Liu, Z. Liu, D. Wang, M. A. Camburn, J. C. Fang, R. Hao, X. Fang, S. Zheng, N. Hu and X. Wang, *Nat Commun*, 2019, **10**, 3862.
14. N. Matsuhisa, Y. Jiang, Z. Liu, G. Chen, C. Wan, Y. Kim, J. Kang, H. Tran, H. C. Wu, I. You, Z. Bao and X. Chen, *Adv. Electron. Mater.*, 2019, **5**, 1900347.
15. S. Gong, L. W. Yap, B. Zhu, Q. Zhai, Y. Liu, Q. Lyu, K. Wang, M. Yang, Y. Ling, D. T. H. Lai, F. Marzbanrad and W. Cheng, *Adv. Mater.*, 2019, **31**, e1903789.
16. B. Zhang, J. Lei, D. Qi, Z. Liu, Y. Wang, G. Xiao, J. Wu, W. Zhang, F. Huo and X. Chen, *Adv. Funct. Mater.*, 2018, **28**, 1801683.
17. G. Chen, N. Matsuhisa, Z. Liu, D. Qi, P. Cai, Y. Jiang, C. Wan, Y. Cui, W. R. Leow, Z. Liu, S. Gong, K. Q. Zhang, Y. Cheng and X. Chen, *Adv. Mater.*, 2018, **30**, e1800129.
18. H. B. Lee, C. W. Bae, T. Duy le, I. Y. Sohn, D. I. Kim, Y. J. Song, Y. J. Kim and N. E. Lee, *Adv. Mater.*, 2016, **28**, 3069-3077.
19. R. Guo, Y. Yu, J. Zeng, X. Liu, X. Zhou, L. Niu, T. Gao, K. Li, Y. Yang, F. Zhou and Z. Zheng, *Adv. Sci*, 2015, **2**, 1400021.
20. Y. Zhao, D. Dong, S. Gong, L. Brassart, Y. Wang, T. An and W. Cheng, *Adv. Electron. Mater.*, 2018, **5**, 1800462.
21. T. Zhu, K. Wu, Y. Xia, C. Yang, J. Chen, Y. Wang, J. Zhang, X. Pu, G. Liu and J. Sun, *Nano Lett.*, 2022, **22**, 6637-6646.
22. Z. Liu, H. Wang, P. Huang, J. Huang, Y. Zhang, Y. Wang, M. Yu, S. Chen, D. Qi, T. Wang, Y. Jiang, G. Chen, G. Hu, W. Li, J. Yu, Y. Luo, X. J. Loh, B. Liedberg, G. Li and X. Chen, *Adv. Mater.*, 2019, **31**, e1901360.
23. D. Kang, P. V. Pikhitsa, Y. W. Choi, C. Lee, S. S. Shin, L. Piao, B. Park, K. Y. Suh, T. I. Kim and M. Choi, *Nature*, 2014, **516**, 222-226.

24. B. Park, J. Kim, D. Kang, C. Jeong, K. S. Kim, J. U. Kim, P. J. Yoo and T. I. Kim, *Adv. Mater.*, 2016, **28**, 8130-8137.
25. X. Wu, H. Chen, X. Luo, D. Wang, P. Schaaf and G. Zhang, *Adv. Mater. Technol.*, 2021, **6**, 2100524.
26. T. Yang, X. Li, X. Jiang, S. Lin, J. Lao, J. Shi, Z. Zhen, Z. Li and H. Zhu, *Mater. Horizons*, 2016, **3**, 248-255.
27. J. D. Pegan, J. Zhang, M. Chu, T. Nguyen, S. J. Park, A. Paul, J. Kim, M. Bachman and M. Khine, *Nanoscale*, 2016, **8**, 17295-17303.
28. T. Sun, B. Feng, J. Huo, Y. Xiao, J. Peng, Z. Li, W. Wang, L. Liu, G. Zou and W. Wang, *Mater Horiz*, 2023, **10**, 2525-2534.
29. Z. Jiang, N. Chen, Z. Yi, J. Zhong, F. Zhang, S. Ji, R. Liao, Y. Wang, H. Li, Z. Liu, Y. Wang, T. Yokota, X. Liu, K. Fukuda, X. Chen and T. Someya, *Nat Electron*, 2022, **5**, 784-793.
30. Y. Jiang, S. Ji, J. Sun, J. Huang, Y. Li, G. Zou, T. Salim, C. Wang, W. Li, H. Jin, J. Xu, S. Wang, T. Lei, X. Yan, W. Y. X. Peh, S. C. Yen, Z. Liu, M. Yu, H. Zhao, Z. Lu, G. Li, H. Gao, Z. Liu, Z. Bao and X. Chen, *Nature*, 2023, **614**, 456-462.
31. D. Yang, G. Tian, C. Liang, Z. Yang, Q. Zhao, J. Chen, C. Ma, Y. Jiang, N. An, Y. Liu and D. Qi, *Adv. Funct. Mater.*, 2023, **33**, 2300412.
32. H. Li, F. Han, L. Wang, L. Huang, O. W. Samuel, H. Zhao, R. Xie, P. Wang, Q. Tian, Q. Li, Y. Zhao, M. Yu, J. Sun, R. Yang, X. Zhou, F. Li, G. Li, Y. Lu, P. Guo and Z. Liu, *Adv. Funct. Mater.*, 2023, **33**, 2300859.
33. J. L. Beuth and JR, *Int. J. Solids Structures* 1992, **29**, 1657-1675.
34. H. Liang, J. Xu, D. Zhou, X. Sun, S. Chu and Y. Bai, *Ceramics International*, 2016, **42**, 2642-2647.
35. I. Petrov, P. B. Barna, L. Hultman and J. E. Greene, *J. Vac. Sci. Technol. A* 2003, **21**, 117-128.
36. H. Kim, S. Nam, A. Roh, M. Son, M.-H. Ham, J.-H. Kim and H. Choi, *International Journal of Refractory Metals and Hard Materials*, 2019, **80**, 286-291.
37. T. Broom, *Advances in Physics*, 1954, **3**, 26-83.
38. W. Huo, X. Liu, S. Tan, F. Fang, Z. Xie, J. Shang and J. Jiang, *Applied Surface Science*, 2018, **439**, 222-225.
39. K. T. Kashyap, A. Bhat, P. G. Koppad and K. B. Puneeth, *Computational Materials Science*, 2012, **56**, 172-173.
40. Z. Wu, H. Bei, G. M. Pharr and E. P. George, *Acta Mater.*, 2014, **81**, 428-441.
41. N. Lu, Z. Suo and J. J. Vlassak, *Acta Mater.*, 2010, **58**, 1679-1687.
42. J. Lia, P. K. Liawf, Y. Chena, X. X. , H. Wang, C. Jianga, B. Liud, Q. Fang, Y. Liu, Y. Yang, P. K. Liaw and C. T. Liue, *Proc. Natl Acad. Sci. USA*, 2022, **119**, e2200607119.
43. T. J. Jang, W. S. Choi, D. W. Kim, G. Choi, H. Jun, A. Ferrari, F. Körmann, P.-P. Choi and S. S. Sohn, *Nat Commun*, 2021, **12**, 4703.
44. Q. Fang, W. Lu, Y. Chen, H. Feng, P. K. Liaw and J. Li, *J Mech Phys Solids*, 2022, **169**, 105067.
45. T. Sekitani, Y. Noguchi, K. Hata, T. Fukushima, T. Aida and T. Someya, *Science*, 2008, **321**, 1468-1472.
46. S. Liu, D. S. Shah and R. Kramer-Bottiglio, *Nat Mater*, 2021, **20**, 851-858.
47. N. Matsuhisa, D. Inoue, P. Zalar, H. Jin, Y. Matsuba, A. Itoh, T. Yokota, D. Hashizume and T. Someya, *Nat Mater*, 2017, **16**, 834-840.
48. Y. Wang, C. Zhu, R. Pfattner, H. Yan, L. Jin, S. Chen, F. Molina-Lopez, F. Lissel, J. Liu, N. I. Rabiah, Z. Chen, J. W. Chung, C. Linder, M. F. Toney, B. Murmann and Z. Bao, *Sci Adv*, 2017, **3**, e1602076.
49. S. Choi, S. I. Han, D. Jung, H. J. Hwang, C. Lim, S. Bae, O. K. Park, C. M. Tschabrunn, M. Lee, S. Y. Bae, J. W. Yu, J. H. Ryu, S. W. Lee, K. Park, P. M. Kang, W. B. Lee, R. Nezafat, T. Hyeon and D. H. Kim, *Nat Nanotechnol*, 2018, **13**, 1048-1056.
50. F. Sun, M. Tian, X. Sun, T. Xu, X. Liu, S. Zhu, X. Zhang and L. Qu, *Nano Lett.*, 2019, **19**, 6592-6599.
51. J. Zhou, G. Tian, G. Jin, Y. Xin, R. Tao and G. Lubineau, *Adv. Funct. Mater.*, 2019, **30**, 1907316.
52. Y. Ohm, C. Pan, M. J. Ford, X. Huang, J. Liao and C. Majidi, *Nat Electron*, 2021, **4**, 185-192.

53. Y. Kim, J. Zhu, B. Yeom, M. Di Prima, X. Su, J. G. Kim, S. J. Yoo, C. Uher and N. A. Kotov, *Nature*, 2013, **500**, 59-63.
54. E. J. Markvicka, M. D. Bartlett, X. Huang and C. Majidi, *Nat Mater*, 2018, **17**, 618-624.
55. C. Choi, J. M. Lee, S. H. Kim, S. J. Kim, J. Di and R. H. Baughman, *Nano Lett.*, 2016, **16**, 7677-7684.
56. M. Kong, I. You, G. Lee, G. Park, J. Kim, D. Park and U. Jeong, *Adv. Mater.*, 2021, **33**, e2100299.
57. X. Li, M. Li, J. Xu, J. You, Z. Yang and C. Li, *Nat Commun*, 2019, **10**, 3514.
58. Z. Chen, W. Ren, L. Gao, B. Liu, S. Pei and H. M. Cheng, *Nat Mater*, 2011, **10**, 424-428.
59. G. Li, K. Huang, J. Deng, M. Guo, M. Cai, Y. Zhang and C. F. Guo, *Adv. Mater.*, 2022, **34**, e2200261.
60. Y. Lia, T. Fang, J. Zhang, H. Zhua, Y. Suna, S. Wang, Y. Lua and D. Kong, *Proc. Natl Acad. Sci. USA*, 2023, **121**, e2300953120.